

## Experimental studies of coherent structures in an advection-reaction-diffusion system

Savannah Gowen and Tom Solomon

Citation: *Chaos* **25**, 087403 (2015); doi: 10.1063/1.4918594

View online: <http://dx.doi.org/10.1063/1.4918594>

View Table of Contents: <http://scitation.aip.org/content/aip/journal/chaos/25/8?ver=pdfcov>

Published by the [AIP Publishing](#)

---

### Articles you may be interested in

[Pinning of reaction fronts by burning invariant manifolds in extended flows](#)

*Phys. Fluids* **27**, 023601 (2015); 10.1063/1.4913380

[Dependence of advection-diffusion-reaction on flow coherent structures](#)

*Phys. Fluids* **25**, 106602 (2013); 10.1063/1.4823991

[Influence of a simple magnetic bar on buoyancy-driven fingering of traveling autocatalytic reaction fronts](#)

*Phys. Fluids* **24**, 124101 (2012); 10.1063/1.4768722

[Influence of temperature on linear stability in buoyancy-driven fingering of reaction-diffusion fronts](#)

*Chaos* **22**, 037107 (2012); 10.1063/1.4753924

[Interaction between buoyancy and diffusion-driven instabilities of propagating autocatalytic reaction fronts. I. Linear stability analysis](#)

*J. Chem. Phys.* **130**, 114502 (2009); 10.1063/1.3077180

---



# Experimental studies of coherent structures in an advection-reaction-diffusion system

Savannah Gowen<sup>a)</sup> and Tom Solomon<sup>b)</sup>

*Department of Physics and Astronomy, Bucknell University, Lewisburg, Pennsylvania 17837, USA*

(Received 19 December 2014; accepted 6 April 2015; published online 9 June 2015)

We present experimental studies of reaction front propagation in a single vortex flow with an imposed external wind. The fronts are produced by the excitable, ferroin-catalyzed Belousov-Zhabotinsky chemical reaction. The flow is generated using an electromagnetic forcing technique: an almost-radial electrical current interacts with a magnetic field from a magnet below the fluid layer to produce the vortex. The magnet is mounted on crossed translation stages allowing for movement of the vortex through the flow. Reaction fronts triggered in or in front of the moving vortex form persistent structures that are seen experimentally for time-independent (constant motion), time-periodic, and time-aperiodic flows. These results are examined with the use of *burning invariant manifolds* that act as one-way barriers to front motion in the flows. We also explore the usefulness of finite-time Lyapunov exponent fields as an instrument for analyzing front propagation behavior in a fluid flow. © 2015 AIP Publishing LLC. [<http://dx.doi.org/10.1063/1.4918594>]

During the past few decades, numerous studies have indicated the importance of well-defined coherent structures in the dynamics of fluid systems. In particular, studies of *chaotic mixing*<sup>1,2</sup> led to the development of mathematical and topological tools<sup>3,4</sup> for characterizing mixing in time-independent and time-periodic velocity fields. More recently, these ideas have been extended to more complicated flows,<sup>5–12</sup> including aperiodic and even turbulent flows similar to those found in oceans and atmospheres.<sup>8,13</sup> Mixing also plays a crucial role on reaction behavior in laminar flows.<sup>14–22</sup> The generalized *advection-reaction-diffusion* (ARD) problem is one with significant applications to a wide range of systems, spanning the fields of physics, biology, chemistry, geophysics, astrophysics and chemical and mechanical engineering. In this paper, we present experiments on the propagation of reaction fronts in a flow composed of a single vortex with an imposed wind. This flow is chosen for its simplicity, which should facilitate theoretical analysis. With the addition of the wind, reaction fronts typically pin to the vortex with a persistent front shape. We explain these patterns with the use of recent *burning invariant manifold* (BIM) theories<sup>22–24</sup> that extend the tools that were developed for passive mixing to the more general ARD problem. We examine persistent front shapes for time-independent and time-periodic flows and compare the shapes with BIMs calculated from the measured velocity field. We also consider reaction patterns with time-aperiodic forcing. We calculate finite-time Lyapunov exponent (FTLE) fields for sections of the three-dimensional phase space of reaction fronts, and speculate about the applicability of FTLE techniques to ARD systems.

## I. INTRODUCTION

Coherent structures play a significant role in the dynamics of a wide range of fluid systems. Persistent structures in velocity fields (Eulerian Coherent Structures) are found not only for smooth, laminar flows, but have also been identified for turbulent flows. Examples of Eulerian coherent structures include the jet stream in the atmosphere and the Gulf Stream in the Atlantic Ocean; large vortices such as Agulhas Rings<sup>25</sup> that persist in the oceans for months and sometimes years; and Jupiter's Great Red Spot,<sup>26</sup> which is a large vortex structure that has persisted for at least 350 years in an extremely turbulent environment. During the past few decades, concepts of coherent structures have been applied<sup>2,5</sup> to studies of fluid mixing and transport. Specifically, transport barriers form that result in unmixed regions which can persist for long periods of time. For time periodic 2D flows and time-independent 3D flows, Kolmogorov-Arnold-Moser (KAM) theory<sup>2</sup> describes the separation of the fluid system into regions of ordered and chaotic trajectories, separated by impermeable transport barriers. Furthermore, invariant manifolds connected to fixed points in the flow act as mixing barriers. Lobes or turnstiles formed from the intersections of these manifolds<sup>4,27–31</sup> control the long-range transport of passive impurities in the flow.

During the past decade, techniques have been developed to characterize and predict mixing barriers that form even if the flow is aperiodic or turbulent, flows for which KAM and manifold theory do not rigorously apply. The expression Lagrangian Coherent Structures (LCS)<sup>5</sup> denotes these persistent transport structures, although the term LCS could equally apply to any persistent mixing region bounded by transport barriers in a flow.

Mixing has a profound impact on processes that occur in fluid flows; consequently, Lagrangian coherent structures are important for a wide range of applications. Here, we focus on ARD systems; i.e., those with both fluid mixing and reaction behavior. Persistent, coherent structures are prevalent in

<sup>a)</sup>Current address: Department of Physics, Mount Holyoke College, South Hadley, Massachusetts 01075, USA.

<sup>b)</sup>Electronic mail: [tsolomon@bucknell.edu](mailto:tsolomon@bucknell.edu)

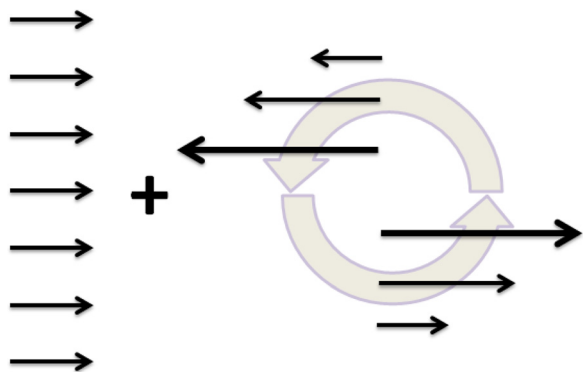


FIG. 1. Cartoon sketch of the single vortex flow with an imposed wind.

ARD systems; patterns are often formed by the reactions, especially if the reaction is oscillatory<sup>32</sup> or if the flow is open with sources and sinks.<sup>33,34</sup> Persistent structures also form in reaction front propagation in a fluid flow. This is a problem with significant applications for a wide range of systems, including wildfires, plankton blooms,<sup>35,36</sup> microfluidic chemical reactors<sup>37</sup> and medical assay devices, interacting plasma systems,<sup>38</sup> phase transitions in matter,<sup>39</sup> cellular- or embryonic-scale biological systems<sup>40,41</sup> and the spreading of a disease in a moving population.<sup>42</sup>

In this paper, we present experiments on persistent front propagation patterns in an ARD system. A simple flow is chosen to make it easier to clarify and identify the structures that control the reaction behavior; specifically, we use a single vortex flow with an imposed wind (Fig. 1). We study time-independent, time-periodic and time-aperiodic flows. The reaction is the excitable Belousov-Zhabotinsky chemical reaction,<sup>43-45</sup> a reaction which produces pulse-like fronts and which has been studied extensively in the past in the reaction-diffusion (no flow) regime. We discuss how the patterns made by these fronts can be characterized and predicted, focusing in particular on BIMs which are an extension of the passive manifolds to the ARD case. BIMs form one-way barriers that impede the motion of reaction fronts and, in many cases, determine the shape of any persistent front structures. We also explore the utility of FTLE fields in analyzing the reaction structures observed experimentally.

In Sec. II, we provide background about passive invariant manifolds that control mixing in laminar flows, and recent theories of burning invariant manifolds that extend these ideas to ARD systems. In Sec. III, we describe the experimental techniques. Section IV presents the experimental results, focusing on persistent front patterns observed in the time-independent and time-periodic regimes. We compare these patterns to BIMs calculated numerically from the velocity field. In Sec. V, we present calculations of “burning-FTLE” fields and speculate on the applicability of this technique for elucidating coherent structures in a range of flows. We discuss these results and continuing work in Sec. VI.

## II. BACKGROUND

Long-range transport of a passive impurity in time-independent or weakly time-periodic flows is governed by

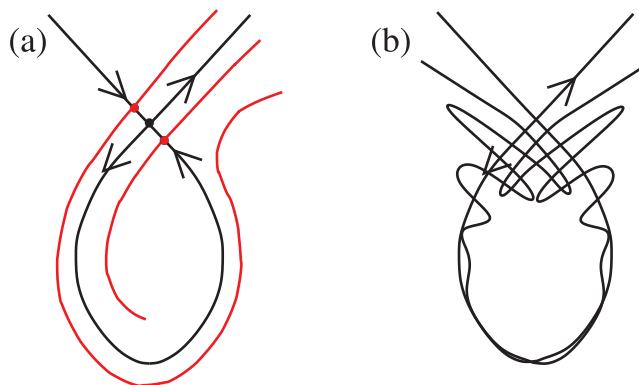


FIG. 2. Cartoon sketch of fixed points and manifolds for the single vortex flow with an imposed wind. (a) Time-independent flow. The black dot and the black curve are the fixed point and manifolds for passive mixing, and the red dots and red curves are burning fixed points and burning invariant manifolds for front propagation in the same flow. (b) Time-periodic flow; only the passive invariant manifolds are shown.

passive invariant manifolds attached to (Eulerian) fixed points in the flow.<sup>30,31,46,47</sup> Figure 2 shows the Eulerian fixed point (black dot) and its associated manifolds for a single vortex with an imposed horizontal wind. For a time-independent flow (Fig. 2(a)), there is one fixed point with a homoclinic manifold structure. The manifold separates the flow into three distinct mixing regions: a region within the body of the “fish” in which tracers undergo closed loops, and two regions outside of the fish where trajectories are unbounded.

The addition of lateral, time-periodic oscillations (perpendicular to the wind) results in chaotic mixing (Fig. 2(b)). The unstable and stable manifolds attached to the Eulerian fixed point are no longer coincident and have a succession of stretches and folds typically found in systems with chaotic mixing. Overlapping of these manifolds reveals a pattern of lobes (or “turnstile”)<sup>4,27,28</sup> that allows for mixing into and out of the central region. Previous theory<sup>47</sup> and experiments<sup>30,31</sup> analyzed manifolds and lobes for a time-dependent vortex chain and demonstrated enhanced diffusive mixing with an effective diffusion coefficient that depends on the sizes of the lobes.

An autocatalytic reaction front triggered in a stagnant fluid propagates relative to the fluid at a speed  $V_0$ , determined by Fisher-Kolmogorov-Petrovskii-Piskunov (FKPP) theory<sup>48,49</sup> for “pulled” reaction fronts. If the fluid is moving, the front is also carried advectively by the flow. To model a propagating reaction front in a flow, we employ a theory<sup>22,23</sup> that considers the evolution of an infinitesimal front element. For a two-dimensional (2D) flow, this element is denoted by its  $x$ - and  $y$ -coordinates and by the angle  $\theta$  that a tangent to the front makes with respect to the positive  $x$ -axis. A front element described by the coordinates  $(x, y, \theta)$  can be advected by the flow, can “burn” with a velocity  $V_0$  relative to the fluid in a direction perpendicular to the front, or can be rotated by a combination of vorticity and strain in the flow. (Front elements can also be stretched, a process that is relevant to a finite-time Lyapunov exponent analysis discussed in Sec. V.) These processes are summarized by a 3D set of ordinary differential equations

$$\dot{x} = u_x + v_0 \sin \theta, \quad \dot{y} = u_y - v_0 \cos \theta, \quad (1a)$$

$$\dot{\theta} = (u_{y,y} - u_{x,x}) \sin \theta \cos \theta - u_{x,y} \sin^2 \theta + u_{y,x} \cos^2 \theta. \quad (1b)$$

Equation 1(b) is a special case of the Jeffery Equation<sup>50,51</sup> for rotation of an ellipsoidal tracer in a 2D flow in the case where the aspect ratio of the tracer is infinite, i.e., for a thin rod (or a front element in our case). The non-dimensional front propagation speed  $v_0 \equiv V_0/U$  is a measure of the relative importance of the reaction-diffusion dynamics (quantified by the speed  $V_0$  at which a front propagates in the absence of a fluid flow) and advection (quantified by the characteristic flow speed  $U$ ). In the limit  $v_0 \rightarrow 0$ , advection dominates and reaction fronts are advected with the flow as passive tracers. In the limit  $v_0 \rightarrow \infty$ , reaction-diffusion processes dominate and fronts propagate as though there is no flow. For reference, the same behavior can be parametrized by the Damkohler number  $Da = L/(U\tau_r)$  and the Peclet number  $Pe = UL/D$ , where  $L$  is a characteristic length scale of the flow,  $\tau_r$  is the reaction time scale, and  $D$  is the molecular diffusivity of the reactants. Since FKPP theory<sup>48,49</sup> predicts a reaction-diffusion front speed  $V_0 = 2\sqrt{D/\tau_r}$ , the non-dimensional front speed  $v_0$  can be written in terms of  $Da$  and  $Pe$  as  $v_0 = 2\sqrt{Da/Pe}$ .

The evolution of a front element governed by Eqs. (1) traces out a trajectory in the 3D  $(x, y, \theta)$  phase space. Fixed points in this 3D phase space are called *burning fixed points*. Attached to these fixed points are manifolds called BIMs. In a 2D phase space, invariant manifolds act as impenetrable barriers. In general, however, a 1D invariant manifold in a 3D phase space does not act as a barrier since trajectories can go around the curve. However, the  $\theta$ -coordinate in this particular 3D phase space is not entirely independent of the  $x$  and  $y$  coordinates due to a front compatibility criterion<sup>24</sup> when considering the evolution of an entire front and not just an infinitesimal element.

If the burning fixed points and BIMs are projected onto the 2D,  $(x, y)$  space, we can understand their effects on propagating reaction fronts. Consider a front triggered at the Eulerian fixed point (black dot in Fig. 2(a)). By definition, the fluid is motionless at this fixed point, but the reaction front can move relative to the fluid. The front spreads out from the fixed point, moving away not only along the direction of the unstable manifold, but also outward against the stable manifold. The outward propagation in the stable direction stops when the inward-directed flow matches the outward front propagation speed  $V_0$  relative to the flow. This marks the location of the 2D projection of the burning fixed point (red dots in Fig. 2(a)). However, in 2D, this is a fixed point only for reaction fronts propagating away from the Eulerian fixed point. A front propagating toward the Eulerian fixed point passes through a burning fixed point on the stable passive manifold since the front propagation and fluid velocity both point in the same direction.

Similarly, when projected into  $(x, y)$  space, the BIMs act as barriers only for reaction fronts moving in one direction, whereas opposing fronts pass through. The top/outer BIM in Fig. 2(a), for instance, blocks reaction fronts propagating outward, whereas the other BIM blocks fronts propagating

inward. The one-way nature of the BIMs as barriers in 2D flows has been demonstrated both experimentally and theoretically in previous studies<sup>22–24</sup> for chains of vortices and spatially disordered flows.

### III. EXPERIMENTAL TECHNIQUES

#### A. The flow

The flow is generated using electromagnetic forcing techniques (Fig. 3). A thin (2.5 mm) fluid layer is confined in a rectangular box. A 15 cm diameter Nd-Fe-B magnet sits just below the box, mounted on two perpendicular translation stages. An electrical current passes between an electrode that dips into the fluid just above the center of the magnet and a second electrode that surrounds the inner edge of the box. The mostly radial current interacts with the magnetic field from the Nd-Fe-B magnet to produce a single vortex.

To measure the velocity field for the vortex, we scatter a couple of 500 micron polystyrene particles on the surface of the fluid; a small number is used to avoid clumping of tracers on the surface. The particles are black and the background is white to enable easy tracking (using a CCD camera with an acquisition rate of 15 fps) as they follow mostly closed circles around the vortex. (The tracers have a slightly higher density than the fluid so there is a very slight outward spiraling over many rotations.) Since the base vortex flow is time independent, these measurements are repeated many times with the tracers at different distances from the electrode, and the obtained velocities are combined. The radial component of the velocity field is negligible, and the azimuthal component (Fig. 4)  $v_\theta$  is described quite well by a  $1/r$  relationship out almost to the radius of the magnet (for  $r$  up to a crossover radius  $r_c = 7.20$  cm). The velocities aren't measured within a centimeter of the point electrode due to inertial effects. There is a small range of radii near and beyond the edge of the magnet where there is a weak flow reversal due to fringing of the magnetic field.

For  $r < r_c$ , the flow velocities scale linearly with the forcing current  $I$ . This is demonstrated in Fig. 4 by plotting the data for three different forcing currents, with the velocities scaled by  $I/I_0$ , where  $I_0 = 1.67$  mA is the current for one of the three data sets. This scaling does not hold as well in the weak flow reversal region. In all of the BIM calculations, we model the azimuthal velocity as  $A/r$  for  $r < r_c$ , as a third-order polynomial from  $r = r_c$  up to a radius  $r_0 =$

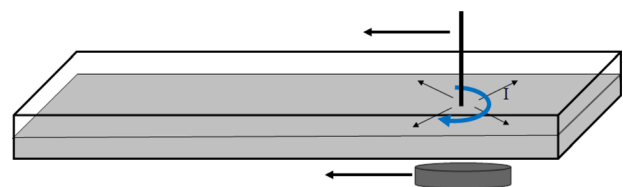


FIG. 3. Flow apparatus. A 58 cm by 28 cm acrylic box has a 2.5 mm thick fluid layer, underneath which sits a Nd-Fe-B magnet with radius  $R = 7.5$  cm, mounted on two crossed translation stages. An electrical current passes between a point electrode above the magnet and a second electrode surrounding the box. Interaction of this current with the magnetic field produces the vortex flow.

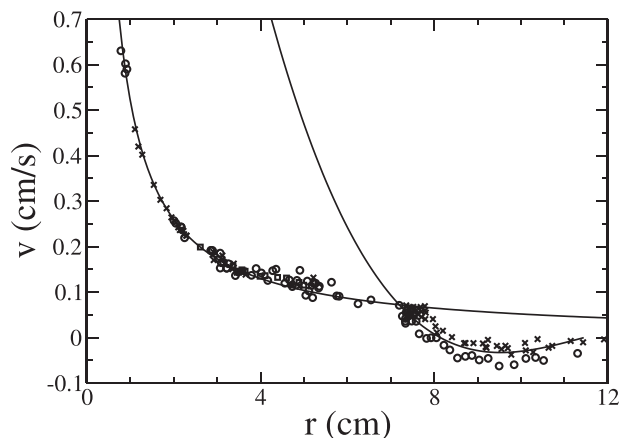


FIG. 4. Azimuthal velocity. Experimental measurements are shown for driving current  $I=0.83$  mA (circles), 1.67 mA (crosses), and 3.35 mA (squares). The velocities are scaled by a factor  $I/I_0$  where  $I_0=1.67$  mA. The solid curves show the fits  $A/r$  (with  $A=0.52\text{cm}^2/\text{s}$ ) for  $r < r_c$  where  $r_c=7.20$  cm, and  $a_0 + a_1r + a_2r^2 + a_3r^3$  (with  $a_0=3.28$ ,  $a_1=-0.913$ ,  $a_2=0.0822$ , and  $a_3=-0.0024$ , all in units of cm and s) for  $r$  between  $r_c$  and  $r_o=11.47$  cm.

11.47 cm where the flow returns approximately to zero, and zero for all radii  $r > r_o$ .

Although we model the flow as 2D, there are some 3D components that are not included in the model. First, there is the no-slip boundary condition at the bottom of the fluid layer. Not only does this result in a boundary layer at the bottom where the fluid speed drops to zero, but it also causes Ekman pumping<sup>52</sup> that produces a weak secondary flow that circulates up through the vortex center. Second, electrolysis at the point electrode can cause a weak flow that results in an additional 3D component to the flow and possible deviations from the  $1/r$  scaling near the electrode.

Two translation stages move the magnet underneath the box. One stage moves with a constant speed  $W$ , resulting in motion of the vortex with the same speed  $W$ . In a reference frame moving with the vortex, the flow is a stationary vortex (with velocity field described by Fig. 4) with an additional imposed uniform wind with magnitude  $W$ , as sketched in Fig. 1. Time dependence is imposed by moving the second stage (and, consequently, the magnet and the vortex) in a direction perpendicular to the “wind.” The time dependence can take any form; in this paper, we explore both periodic and aperiodic time dependence.

The center electrode moves with the magnet; however, the outer electrode remains fixed. Furthermore, since the outer electrode is rectangular, the current is not perfectly radial. We measured the velocity field at several different locations around the box to see if the deviations from a radial electrical current have an effect on the measured velocity field. We found that the velocity field shown in Fig. 4 holds well in all of the regions visited by the magnet and center electrode. (Deviations become significant only when the distance from one of the ends is comparable to or smaller than the radius of the magnet.)

We scale velocities by an average vortex speed (in the absence of an imposed wind)  $U = \frac{1}{\pi R^2} (\int_0^{2\pi} \int_0^R (A/r) r dr d\theta) = 2A/R$ , where  $R$  is the radius of the magnet. (This is the same

as the azimuthal speed at a distance  $r = R/2$  from the electrode.) We define a non-dimensional wind  $w \equiv W/U$  and a non-dimensional RD front propagation speed  $v_0 \equiv V_0/U$ .

## B. Reaction chemistry

The reaction used is the excitable, ferroin-catalyzed Belousov-Zhabotinsky chemical reaction.<sup>44,53</sup> The recipe used is as follows: in three separate beakers, mix (a) 23.28 g sodium bromate and 94 ml of 1 M sulfuric acid in 220 ml water; (b) 5.22 g Malonic acid in 52 ml water; and (c) 5.22 g sodium bromide in 52 ml water. The three solutions are then mixed together under a vent hood until clear. We then mix in 4 ml ferroin indicator, pour the mixture into the apparatus and wait 1.5 hours while the reaction bubbles. We then stir the contents to reset the reaction to a uniform orange color and to eliminate accumulated bubbles. We then trigger a reaction with a silver wire, producing a bluish propagating reaction front. Periodically during a series of runs, we add more ferroin to improve visualization of the reaction and to help suppress spurious triggers and spontaneous oscillations of the reaction.

For most of the life of the chemicals, the reaction front is pulse-like, relaxing back (behind the leading edge) to its initial (orange) excitable state, which can then be re-triggered. Toward the end of the life of the chemicals, the relaxation time becomes sufficiently long such that the reaction is more “burn-like” and less pulse-like. The propagation speed  $V_0$  for a stagnant fluid is 0.0065 cm/s, with no measured change in time as the chemicals evolve. There is presumably a dependence of  $V_0$  on the curvature of the front,<sup>19</sup> but that dependence appears to be minimal for the curvatures typically encountered in these experiments.

## IV. RESULTS

### A. Passive transport

We use particle tracking to verify the structure of the passive invariant manifolds. Figure 5(a) shows a simulation of passive tracers in the flow, using the measured velocity field of Fig. 4 and an additional wind in the horizontal direction. Three distinct mixing regions are apparent: a trapped region near the middle where tracers circulate asymmetrically around the vortex center, an unbounded region at the top, and another unbounded region below where tracers circumnavigate the trapped region before continuing downstream. These regions are separated by the passive manifolds attached to the flow’s Eulerian fixed point. Experimentally measured streaks for 30 - 40 floating 500 micron particles in the same flow are shown in Fig. 5(b), along with the passive invariant manifolds (shown in red) calculated numerically. The shadow at the bottom is the support holding the electrode.

### B. Reaction fronts—time-independent flow

A sequence of images is shown in Fig. 6 of a front for the vortex with a time-independent wind. After a transient, the reaction front converges to a roughly stationary shape that remains unchanged for the remainder of the experiment. Note

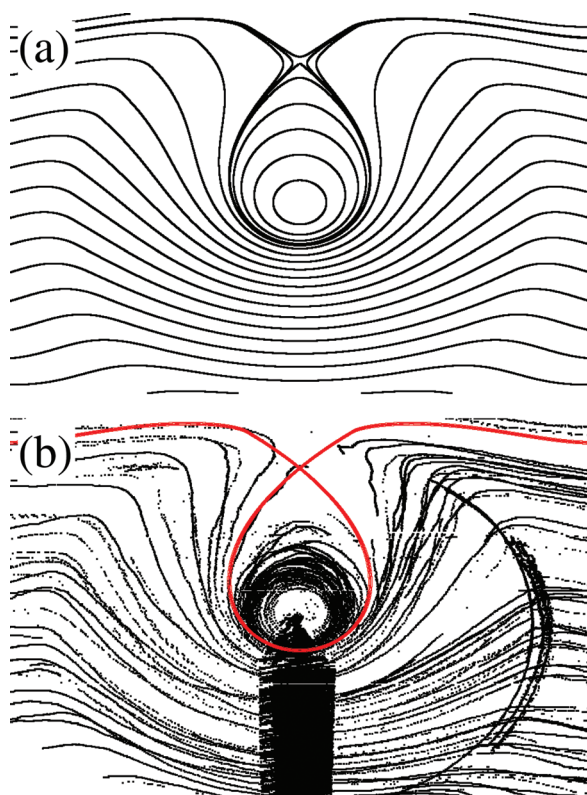


FIG. 5. Motion of passive tracer particles in single vortex flow with an imposed horizontal wind; characteristic vortex velocity  $U = 0.14$  cm/s, dimensionless wind speed  $w = 0.69$  and dimensionless front propagation speed  $v_0 = 0.048$ . (a) Simulated trajectories, based on measured velocity field of Fig. 4. (b) Experimental trajectories, plotted from a reference frame moving with the vortex.

that there is a “shadowing” issue with these images due to the non-slip boundary condition – once the reaction has propagated down to the bottom of the fluid layer, there remains a thin remnant of the reacted fluid left behind after the vortex moves past, even in regions where simulations of the ARD behavior would predict unreacted fluid.

Pinning of reaction fronts similar to that in Fig. 6 has been observed in previous experimental studies.<sup>54</sup> This pinning can be explained by BIM theory. Fig. 7 shows the pinned reaction fronts for three different non-dimensional front propagation speeds  $v_0$ ,<sup>55</sup> along with BIMs that have been calculated numerically from the same flow. Figures 7(a)–7(c) show averaged images (in the co-moving reference frame) taken after the front has achieved a steady state.

There is general agreement between the experimental results (Figs. 7(a)–7(c)) and the predicted BIMs (Figs. 7(d)–7(f)), although there are, of course, small differences due to the approximations made in the model (discussed in Sec. III A). There are several things to note. First, the BIMs are more separated from the passive invariant manifolds (red curves in Figs. 7(d)–7(f)) and from each other for large  $v_0$  (Fig. 7(f)) than for smaller  $v_0$  (Fig. 7(c)). This can be understood by noting that increasing  $v_0$  requires that the burning fixed points move out farther along the stable passive invariant manifolds to find a balance between the outward front propagation and the inward fluid velocity. The BIMs attached to these burning fixed points will also be more separated for larger  $v_0$ . Experimentally, the increased BIM separation for larger  $v_0$  results in a broadening of the steady state, pinned front.

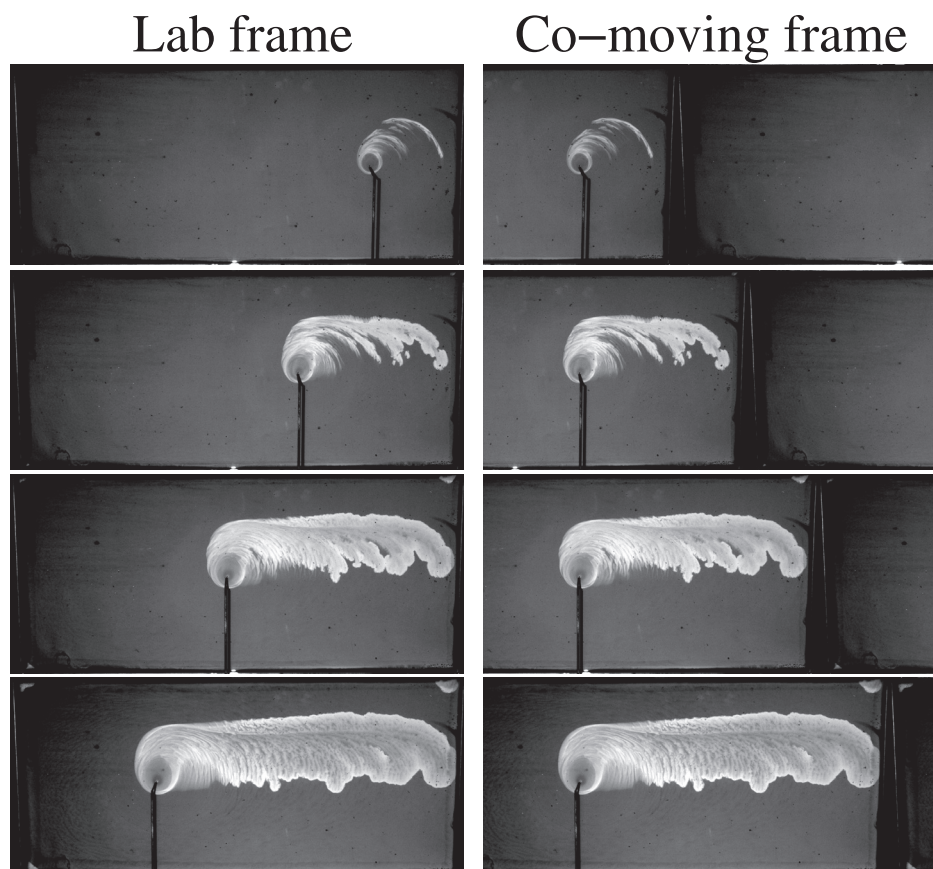


FIG. 6. Sequence of images for reaction front in time-independent flow as viewed both in the lab frame and a frame moving with the vortex;  $U = 0.068$  cm/s,  $v_0 = 0.095$ ,  $w = 0.69$ . Time increases moving downward, with the images spaced by 200 s each.

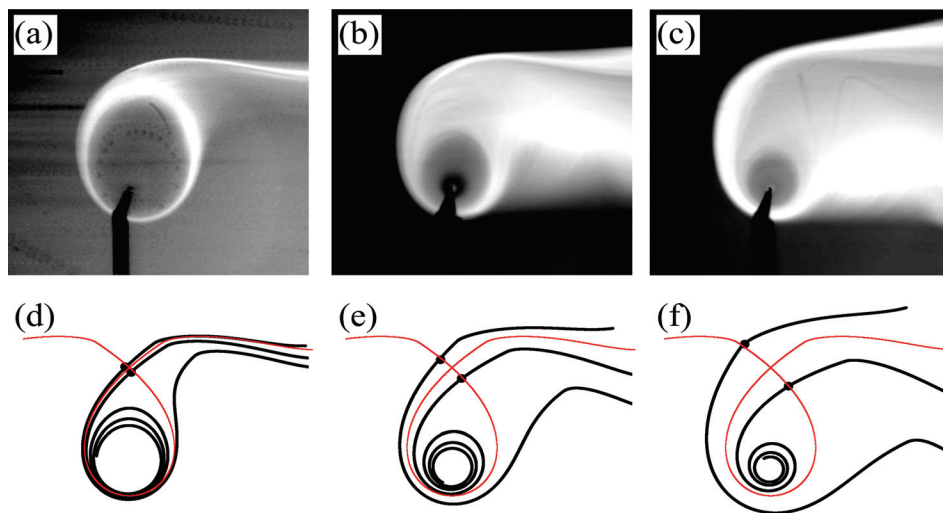


FIG. 7. Persistent reaction patterns for vortex with a steady imposed wind (pointing to the right); all images are viewed in the co-moving reference frame. (a)–(c) Experimental averages of the steady-state front pattern; (d)–(f) calculated BIMs for the same flows. The non-dimensional front and wind speeds  $v_0$  and  $w$  are: 0.024 and 0.69 for (a) and (d); 0.095 and 0.069 for (b) and (e); and 0.19 and 0.69 for (c) and (f). Black dots in (d)–(f) denote location of the burning fixed points, and the red curves denote the passive invariant manifolds.

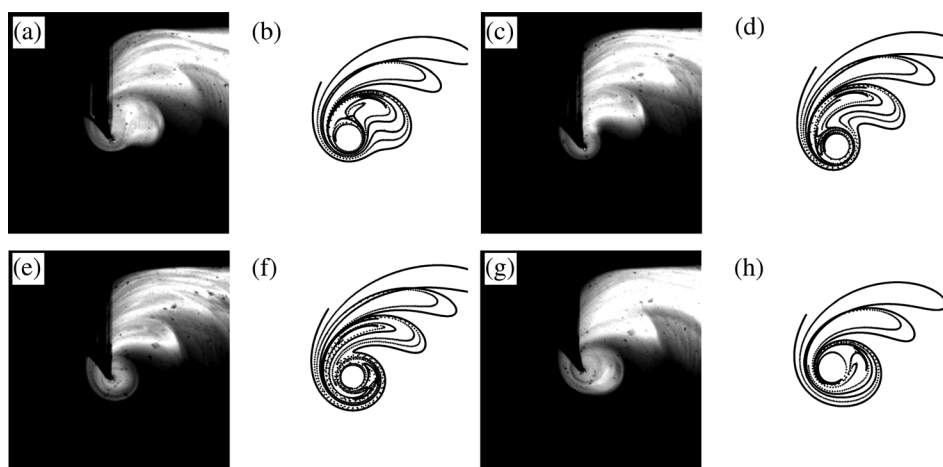


FIG. 8. Experimental images of reaction fronts for time-periodic flow [(a), (c), (e), and (g)], along with BIMs predicted for the same flow parameters [(b), (d), (f), and (h)];  $U = 0.14$  cm/s,  $v_0 = 0.048$ ,  $w = 0.69$ , and the lateral oscillations have amplitude 0.50 cm (0.065 R) and frequency 34 s (0.62 in units of the advective time  $R/U$ ). The images show different phases of the oscillation: 0 (for (a) and (b)),  $\pi/2$  ((c) and (d)),  $\pi$  ((e) and (f)) and  $3\pi/2$  ((g) and (h)).

Second, there is an excluded (darker, unreacted) region in the middle of the persistent structures that decreases in size with increasing  $v_0$ . This can be understood by considering how these fronts are triggered, along with the one-way blocking behavior of the BIMs. The outer BIMs block outward-propagation fronts, whereas the inner BIMs block only inward-propagating fronts. A front triggered near the electrode propagates outward, through the inner BIM, converging and stopping when it reaches the outer BIM. Since the reaction is excitable, the fluid near the vortex core resets back to its orange, pre-triggered state. Fluid near the outside is continually re-triggered, but that re-triggered region has difficulty propagating back into the middle region due to the inner BIMs which block inward-propagating fronts. It should be possible for the front to spiral back toward the center around the spiraling inner BIM, but we do not observe any spiral penetration in the experiments. The decreasing size of the internal hole with increasing  $v_0$  is consistent with the BIM pictures that reveal a tighter and narrower spiral for larger  $v_0$ .

Experiments have also been done where a front is triggered ahead of the advancing vortex (upstream in the co-moving reference frame). The steady state patterns are the same in this case, since the front can penetrate the outer BIM (which blocks only outward propagating fronts), after which the front can then fill in the BIM region from the inside.

### C. Time-periodic flow

Experimental images of fronts for a flow with time-periodic lateral oscillations are shown in Fig. 8, along with numerical calculations of the BIMs for the same flow. Because of the periodic oscillations, we average images taken at the same phase of the lateral oscillations. The results are shown in Fig. 8 at four different phases of the oscillation, along with predicted BIMs for the same conditions. Passive invariant manifolds are not shown in these images; they are similar to the BIMs shown, but slightly retracted toward the center of the vortex, with sharper and deeper fjords (the folds of the BIMs overlap farther out in the fjords due to the broadening). The broadening of the BIMs relative to the passive invariant manifolds is similar to that from the time-independent case; since  $v_0$  for Fig. 8 is twice and one-half those of Figs. 7(d) and 7(e) (respectively), the separation between the BIMs and the passive invariant manifolds in Fig. 8 is roughly twice and one-half of those from Figs. 7(d) and 7(e).

The BIMs are much more complicated for time-periodic flows – as is the case for passive invariant manifolds – since this is a flow that gives rise to chaotic fluid mixing. Nevertheless, the reaction patterns roughly follow the structure of the outermost portions of the BIMs. Similar to the time-independent case, increases in  $v_0$  (not shown in Fig. 8)

cause a broadening of the patterns. For the time-periodic flow, the broadening has the effect of smoothing out the many folds and deep fjords in the patterns seen at smaller  $v_0$ .

#### D. Time-aperiodic forcing

The translation stages can be programmed to execute any arbitrary pattern of motions. We impose time-aperiodic forcing by programming a series of moves with random velocity and displacement in the lateral direction. An advantage of this approach is that even though the forcing is random, we have a detailed record of each displacement that can be used in any analysis. We also have the ability to reproduce a run with precisely the same conditions, or one with all of the velocities scaled by a common factor.

A triggered front at several different times (after an appropriate transient) in a time-aperiodic flow is shown in Fig. 9. The front structures seen in these images never settle down to a steady shape. Nevertheless, there are still clear, identifiable structures visible in these images and the front is still clearly pinned.

Autocatalytic reactions in open flows with chaotic or random time dependence were studied theoretically and

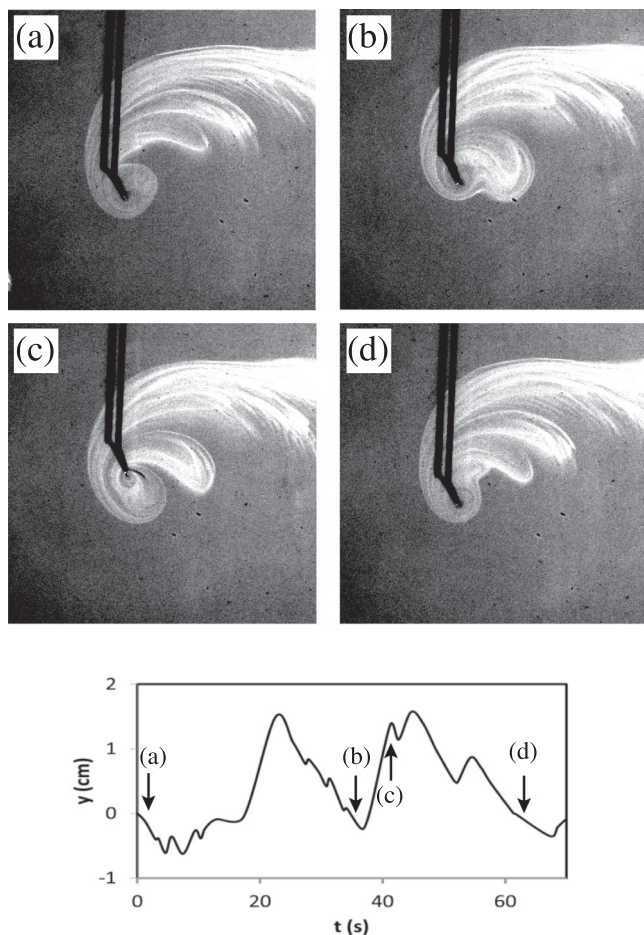


FIG. 9. Reaction fronts in vortex flow with aperiodic time dependence;  $U = 0.14$  cm/s,  $v_0 = 0.048$ ,  $w = 0.69$ . The lateral (up and down) oscillations have a range of 2.2 cm, standard deviation 0.68 cm, 0.42 cm skewness, and 1.04 cm kurtosis. The graph of lateral displacements at the bottom shows a sample of the aperiodic forcing, with arrows indicating the times for the four images.

computationally by Károlyi *et al.*<sup>56</sup> Those studies predicted a singular enhancement in the production rate for the chemical reaction for the random flows, beyond the enhancement found for time-independent and time-periodic flows. The theory in that study was based on the scaling of thin reaction regions surrounding fractal-shaped unstable manifolds of the chaotic saddles that describe mixing in the flow. We are currently studying possible extensions to BIM theory to ascertain how well it can describe the shapes of the coherent reaction structures in time-aperiodic flows. We discuss this in more detail in Sec. V.

#### V. BURNING FINITE-TIME LYAPUNOV EXPONENT FIELDS

The BIM analysis presented in this paper is rigorously valid only for time-independent and time-periodic flows. If we are interested in analyzing coherent reaction structures in aperiodic and turbulent flows, it is necessary to generalize the analysis in a way that (a) captures reaction barriers in a wide range of flows; and (b) captures the BIM behavior already observed in the time-independent and time-periodic regimes.

The desire to identify and predict reactive coherent structures in a wide range of flows parallels the on-going discussion of LCS for passive mixing. Several techniques have been proposed for the LCS problem, including FTLE fields<sup>6,7</sup> which measure local stretching in the flow; hypergraph and mesohyperbolicity techniques;<sup>8</sup> ergodic partition and diffusion map approaches;<sup>9</sup> finite-time curvature fields;<sup>12</sup> variational approaches;<sup>11</sup> and techniques based on Koopman decomposition.<sup>10</sup> An extension of BIM theory based on the variational approaches has been developed by Mahoney and Mitchell and is presented elsewhere.<sup>57</sup>

Here, we present some preliminary results of an FTLE analysis of reaction fronts in the single vortex with an imposed wind. Specifically, we calculate the “burning FTLE” (bFTLE) field, which is the FTLE field based on the 3D ODE system of front element equations (Eqs. (1)). Backward-time bFTLE fields are shown in Figs. 10 and 11. Figure 10(a) shows the  $x - y$  projection of the BIMs for the same conditions as in Figs. 7(b) and 7(e). Cross sections of the 3D bFTLE field are shown in Figs. 10(b)–10(d) for constant values of  $y$ , corresponding to the three dashed lines (in red) in Fig. 10(a). Each cross section covers a range of  $y$  from  $-4.0$  cm to  $+4.0$  cm (in the horizontal direction) and  $\theta$  from  $0$  to  $2\pi$  (in the vertical direction). Figure 11 shows constant- $\theta$  slices of the 3D bFTLE for  $\theta = 0, \pi/2, \pi,$  and  $3\pi/2$  radians, along with the FTLE field for passive mixing for the same flow conditions.

The bFTLE slices in Fig. 10 show structure that matches up quite well with the points where the BIMs cross the  $(y, \theta)$  plane. First, there are two dominant regions in each of the three slices – a light gray region that corresponds to  $(x, y, \theta)$  trajectories that move inward toward the center of the vortex, and a darker region that corresponds to trajectories that move away from the vortex. This demonstrates a significant difference between the 3D ARD problem and the simple transport problem, where the future behavior is determined

only by the initial  $x$  and  $y$  coordinates of the trajectory. Emanating from the light gray region are a series of filaments; the intersections of the brightest of these filaments with the edge of the gray region matches up quite well with the locations of the BIM crossings. Note that Fig. 10(c) is missing two circles – the BIM simulation shown in Fig. 10(a) was stopped before the BIM had wrapped around and crossed the  $x = 1.0$  cm ( $y, \theta$ ) cross section twice more. We have not plotted red circles in Fig. 10(d), since there are an infinite number of BIM crossings through a cross section at  $x = 0.0$ .

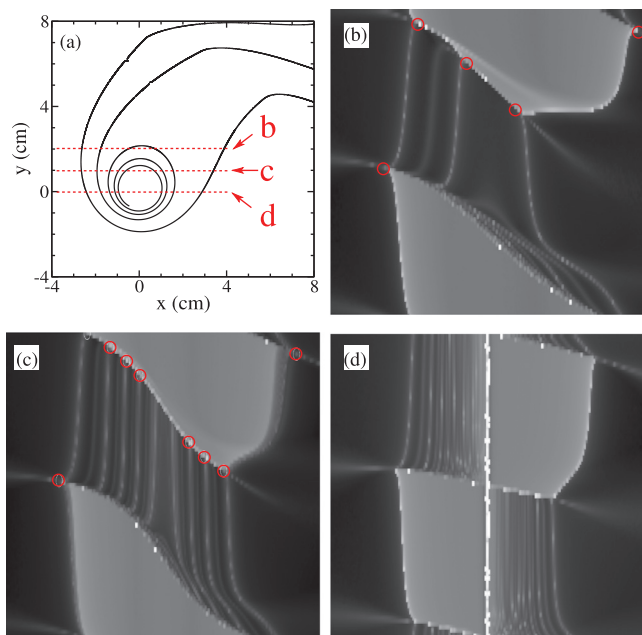


FIG. 10. (a) BIMs for time-independent flow with  $v_0 = 0.095$  and  $w = 0.069$ . The red dashed lines show the  $x$ -values for the cross-sections for the burning-FTLE fields shown in (b)–(d). Burning FTLE fields (for time 1000 s) are shown for the same flow for (b)  $y = 2.0$  cm; (c)  $y = 1.0$  cm; and (d)  $y = 0.0$  cm. The red circles in (b) and (c) show the locations of the intersections of the BIMs from (a) through the  $(x, \theta)$  cross section.

Some caveats are in order. First, the fact that there is a clear correlation between the structures in the bFTLE slices and the BIM intersections does not necessarily mean that the bFTLE fields could be used a priori to *predict* the locations of the BIMs and the shape of the persistent reaction structures. Second, the results presented here are for the simplest kind of flow with only one Eulerian fixed point and no time dependence. It remains to be seen if this approach would provide useful information for more complicated flows. This is an area of ongoing investigation.

Finally, whereas the BIMs are 1D curves in the 3D phase space, the filaments in the bFTLE slices in Fig. 10 are presumably cross sections of 2D sheets permeating the 3D space. To give an idea of the structure in the  $\theta$ -direction, we show slices of the same bFTLE maps in Fig. 11. We do not currently have a complete explanation for these structures or how they can be used to understand front propagation in the 2D flow.

## VI. DISCUSSION

The current study and previous experiments<sup>22,23</sup> indicate that BIMs successfully describe the locations of one-way barriers that impede and, in some cases, block the propagation of reaction fronts in a flow. In this paper, we have chosen a particularly simple flow that demonstrates this behavior, with the goal of providing a simple system for the further analysis of BIMs and their relation to front propagation.

The question of how to extend this analysis to more complicated flows is still unresolved. We have presented some results in Sec. V that indicate that an extension of FTLE approaches to the 3D ARD system might prove to be useful, although the computation times needed for a full 3D analysis might be prohibitive. If the bFTLE approach proves to be useful for analyzing front propagation in flows with a range of time dependence, it will be helpful to determine an

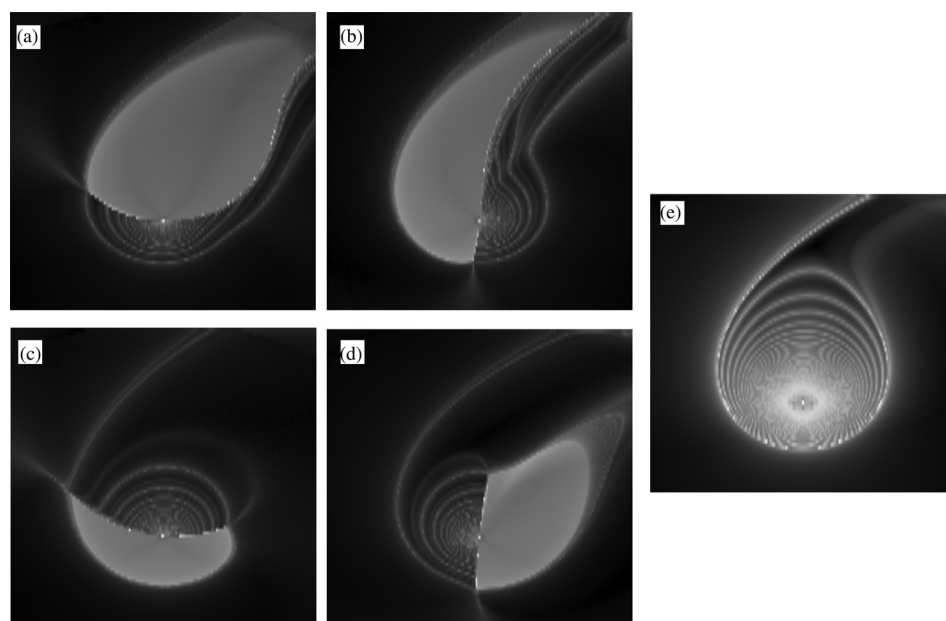


FIG. 11. Burning FTLE slices for constant  $\theta$  for  $v_0 = 0.095$  and  $w = 0.0609$  (same parameters as for Fig. 10). (a)  $\theta = 0$ ; (b)  $\theta = \pi/2$ ; (c)  $\theta = \pi$ ; and (d)  $\theta = 3\pi/2$ . For reference, the passive FTLE is shown in (e) with the same parameters, except that the reaction-diffusion burning speed  $v_0 = 0$ .

approach to reduce the dimensionality of the phase space that needs to be explored.

It is also important to consider the other techniques (mentioned in Sec. V) that are being used to characterize coherent mixing structures in a wide range of flows. We are currently investigating the possibility of extending some of those techniques to the 3D  $(x, y, \theta)$  system. As is the case with the application of those techniques to passive mixing, it is likely that different techniques will elucidate different features of the 3D ARD system.

Recently, there has been significant discussion of frame invariance of techniques used to elucidate coherent transport structures in a fluid flow. Similar questions are relevant when developing theories to characterize coherent reaction structures. Frame invariance is not a concern for time-independent flows – such as the time-independent vortex with wind presented in Sec. IV B—since there is so clearly a preferred reference frame. The same can be said for flows where the time dependence can be expressed as a weak perturbation of a time-independent flow. In fact, manifold theory has been applied quite successfully to characterize passive mixing in these weakly time-dependent regimes, and – as we have shown here and in previous papers – BIM theory successfully describes persistent reaction patterns in these flow regimes. Frame invariance is less trivial if the time dependence is not a weak perturbation. Ultimately, it is our expectation that any passive mixing coherent structure technique extended to the BIM problem will face the same frame-dependent issues as the corresponding passive mixing technique used for 2D flows; e.g., frame invariance (or lack thereof) for bFTLE techniques will be similar to those for FTLE approaches, bLCS techniques will reflect the frame invariance of the variational LCS approaches, etc.

We are continuing experiments with the single vortex flow; in particular, we are investigating flows with different types of time dependence. We are also conducting flows on vortex chains and arrays and on spatially random flows with an imposed time-independent or time-dependent wind. Finally, our ultimate goal is to use the BIM theory to develop an approach for predicting front propagation speeds in arbitrary flows.

## ACKNOWLEDGMENTS

The authors thank John Mahoney and Kevin Mitchell for their assistance in guiding both our theoretical and experimental inquiry in this work. We acknowledge Vered Rom-Kedar for making the suggestion that we explore ARD phenomena in as simple a flow as possible. We also would like to thank Moises Veloz and Jack Raup for assistance with construction of the apparatus. These studies are supported by the U.S. National Science Foundation under Grant Nos. DMR-1004744, DMR-1361881, and PHY-1156964.

<sup>1</sup>H. Aref, *J. Fluid Mech.* **143**, 1 (1984).

<sup>2</sup>J. M. Ottino, *The Kinematics of Mixing: Stretching, Chaos and Transport* (Cambridge University Press, Cambridge, 1989).

<sup>3</sup>E. Ott, *Chaos in Dynamical Systems* (Cambridge University Press, Cambridge, 2002).

- <sup>4</sup>S. Wiggins, *Chaotic Transport in Dynamical Systems* (Springer-Verlag, New York, 1992).
- <sup>5</sup>G. Haller, *Phys. Fluids* **13**, 3365 (2001).
- <sup>6</sup>G. A. Voth, G. Haller, and J. P. Gollub, *Phys. Rev. Lett.* **88**, 254501 (2002).
- <sup>7</sup>M. Mathur, G. Haller, T. Peacock, J. E. Ruppert-Felsot, and H. L. Swinney, *Phys. Rev. Lett.* **98**, 144502 (2007).
- <sup>8</sup>I. Mezic, S. Loire, V. A. Fonoberov, and P. Hogan, *Science* **330**, 486 (2010).
- <sup>9</sup>M. Budisic and I. Mezic, *Physica D* **241**, 1255 (2012).
- <sup>10</sup>M. Budisic, R. Mohr, and I. Mezic, *Chaos* **22**, 047510 (2012).
- <sup>11</sup>M. Farazmand and G. Haller, *Chaos* **23**, 023101 (2013).
- <sup>12</sup>T. Ma and E. Bollt, *SIAM J. Appl. Dyn. Syst.* **13**, 1106 (2014).
- <sup>13</sup>C. Coulliette, F. Lekien, J. D. Paduan, G. Haller, and J. E. Marsden, *Environ. Sci. Technol.* **41**, 6562 (2007).
- <sup>14</sup>Z. Neufeld, C. Lopez, and P. Haynes, *Phys. Rev. Lett.* **82**, 2606 (1999).
- <sup>15</sup>G. Karolyi, A. Pentek, I. Scheuring, T. Tel, and Z. Toroczkai, *Proc. Natl. Acad. Sci. U.S.A.* **97**, 13661 (2000).
- <sup>16</sup>Z. Neufeld, *Phys. Rev. Lett.* **87**, 108301 (2001).
- <sup>17</sup>T. Tel, A. de Moura, C. Grebogi, and G. Karolyi, *Phys. Rep.* **413**, 91 (2005).
- <sup>18</sup>Z. Neufeld, C. Lopez, E. Hernandez-Garcia, and T. Tel, *Phys. Rev. E* **61**, 3857 (2000).
- <sup>19</sup>Z. Neufeld and E. Hernandez-Garcia, *Chemical and Biological Processes in Fluid Flows: A Dynamical Systems Approach* (Imperial College Press, 2009).
- <sup>20</sup>M. S. Paoletti and T. H. Solomon, *Euro. Phys. Lett.* **69**, 819 (2005).
- <sup>21</sup>M. S. Paoletti and T. H. Solomon, *Phys. Rev. E* **72**, 046204 (2005).
- <sup>22</sup>J. Mahoney, D. Bargteil, M. Kingsbury, K. Mitchell, and T. Solomon, *Europhys. Lett.* **98**, 44005 (2012).
- <sup>23</sup>D. Bargteil and T. Solomon, *Chaos* **22**, 037103 (2012).
- <sup>24</sup>K. A. Mitchell and J. R. Mahoney, *Chaos* **22**, 037104 (2012).
- <sup>25</sup>F. J. Beron-Vera, Y. Wang, M. J. Olascoaga, G. J. Goni, and G. Haller, *J. Phys. Oceanogr.* **43**, 1426 (2013).
- <sup>26</sup>P. S. Marcus, *Nature* **331**, 693 (1988).
- <sup>27</sup>R. S. MacKay, J. D. Meiss, and I. C. Percival, *Physica D* **13**, 55 (1984).
- <sup>28</sup>V. Rom-Kedar and S. Wiggins, *Arch. Ration. Mech. Anal.* **109**, 239 (1990).
- <sup>29</sup>V. Rom-Kedar, *Nonlinearity* **7**, 441 (1994).
- <sup>30</sup>T. H. Solomon and J. P. Gollub, *Phys. Rev. A* **38**, 6280 (1988).
- <sup>31</sup>T. H. Solomon, S. Tomas, and J. L. Warner, *Phys. Rev. Lett.* **77**, 2682 (1996).
- <sup>32</sup>C. R. Nugent, W. M. Quarles, and T. H. Solomon, *Phys. Rev. Lett.* **93**, 218301 (2004).
- <sup>33</sup>I. Z. Kiss, J. H. Merkin, and Z. Neufeld, *Physica D* **183**, 175 (2003).
- <sup>34</sup>Z. Toroczkai, G. Karolyi, A. Pentek, T. Tel, and C. Grebogi, *Phys. Rev. Lett.* **80**, 500 (1998).
- <sup>35</sup>A. Scotti and J. Pineda, *J. Mar. Res.* **65**, 117 (2007).
- <sup>36</sup>M. Sandulescu, C. Lopez, E. Hernandez-Garcia, and U. Feudel, *Ecol. Complexity* **5**, 228 (2008).
- <sup>37</sup>T. John and I. Mezic, *Phys. Fluids* **19**, 123602 (2007).
- <sup>38</sup>D. Beule, A. Forster, and T. Fricke, *Zeit. Phys. Chem.* **204**, 1 (1998).
- <sup>39</sup>*Handbook of Crystal Growth*, edited by D. T. J. Hurle (North-Holland, Amsterdam, 1993), Vol. 1B.
- <sup>40</sup>I. Prigogine and I. Stengers, *Order Out of Chaos: Man's New Dialogue with Nature* (Bantam, New York, 1984).
- <sup>41</sup>A. Babloyantz, *Molecular Dynamics and Life: An Introduction to Self-Organization of Matter* (Wiley, New York, 1986).
- <sup>42</sup>C. A. Russell, D. L. Smith, L. A. Waller, J. E. Childs, and L. A. Real, *Proc. R. Soc. London, Ser. B* **271**, 21 (2004).
- <sup>43</sup>L. Kuhnert and H.-J. Krug, *J. Phys. Chem.* **91**, 730 (1987).
- <sup>44</sup>S. K. Scott, *Oscillations, Waves, and Chaos in Chemical Kinetics* (Oxford University Press, Oxford, 1994).
- <sup>45</sup>M. K. R. Reddy, Z. Nagy-Ungvarai, and S. C. Muller, *J. Phys. Chem.* **98**, 12255 (1994).
- <sup>46</sup>V. Rom-Kedar, A. Leonard, and S. Wiggins, *J. Fluid Mech.* **214**, 347 (1990).
- <sup>47</sup>R. Camassa and S. Wiggins, *Phys. Rev. A* **43**, 774 (1991).
- <sup>48</sup>R. A. Fisher, *Ann. Eugenics* **7**, 355 (1937).
- <sup>49</sup>A. N. Kolmogorov, I. G. Petrovskii, and N. S. Piskunov, *Bull. Moscow Univ. Math. Ser. A* **1**, 1 (1937).
- <sup>50</sup>S. Parsa, J. S. Guasto, M. Kishore, N. T. Ouellette, J. P. Gollub, and G. A. Voth, *Phys. Fluids* **23**, 043302 (2011).

- <sup>51</sup>A. Gupta, D. Vincenzi, and R. Pandit, *Phys. Rev. E* **89**, 021001(R) (2014).
- <sup>52</sup>T. H. Solomon and I. Mezić, *Nature* **425**, 376 (2003).
- <sup>53</sup>R. J. Field and M. Burger, *Oscillations and Traveling Waves in Chemical Systems* (Wiley, New York, 1985).
- <sup>54</sup>M. E. Schwartz and T. H. Solomon, *Phys. Rev. Lett.* **100**, 028302 (2008).
- <sup>55</sup>Experimentally, we vary  $v_0$  not by changing the RD front propagation speed  $V_0$  but by changing the characteristic vortex flow speed  $U$  (by changing the current) and the wind speed  $W$  by the same factor.
- <sup>56</sup>G. Karolyi, T. Tel, A. P. de Moura, and C. Grebogi, *Phys. Rev. Lett.* **92**, 174101 (2004).
- <sup>57</sup>J. Mahoney and K. Mitchell, *Chaos* **25**, 087404 (2015).